Inorganic Chemistry

Article

Cite This: Inorg. Chem. 2018, 57, 486−494

pubs.acs.org/IC

A High-Valent Metal-Oxo Species Produced by Photoinduced One-Electron, Two-Proton Transfer Reactivity

Ke Hu,[§,†,‡] Renato N. Sampaio,[§,†] Seth L. Marquard,[†] M. Kyle Brennaman,[†] Yusuke Tamaki,[†] Thomas J. Meyer,[*,†] and Gerald J. Meyer[*,†]

[†]Department of Chemistry, University of North Carolina at Chapel Hill, CB 3290, Chapel Hill, North Carolina 27599, United States

[‡]Department of Chemistry, Fudan University, Shanghai 200433, P. R. China

ABSTRACT: Described herein is a photochemical approach to the generation of a high-valent metal-oxo species that utilizes a chromophore or "sensitizer", a semiconducting electron acceptor, and a redox buffer that poises a catalyst's initial protonation and oxidation state. The photoexcited sensitizer injects an electron into the semiconductor and then oxidizes the catalyst whose reactivity occurs in kinetic competition with back electron transfer. Core−shell SnO_2/TiO_2 semiconductor nanocrystallites inhibited charge recombination relative to TiO_2 acceptors. With low sensitizer-catalyst surface coverages, a novel trapping process is exploited that enables catalysis reactivity to be quantified on time scales ranging from nanoseconds to minutes. A proof-of-principle example provides the demonstration of a light-initiated, ($1e^-$, $2H^+$)-transfer reaction, with an inverse isotope effect of k_H/k_D = 0.63, to generate a Ru(IV) oxo species.

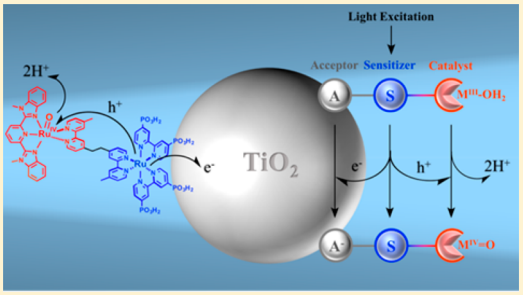

INTRODUCTION

High-valent, metal-oxo species are known to initiate important reactions in chemistry and in the environment such as the oxidation of water.[1−10] For this reason, there has been continued interest in the formation of metal-oxo compounds and in their subsequent reactivity.[11−16] Photons have been utilized to generate metal-oxo species in diffusional reactions[1,2,13,17,18] and through intramolecular metal−oxygen bond-breaking chemistry.[4,19,20] A potential difficulty with the first approach is that diffusion often precludes measurement on short time scales. Direct ligand-to-metal charge-transfer excitation of μ-oxo bridged metal complexes has also been reported to generate high-valent metal-oxo species, but with very low photochemical quantum yields.[1,2,13] Here, we report an alternative light-induced approach for the generation of metal-oxo species that does not require diffusional quenching reactions but rather ultrafast excited-state electron injection into a metal oxide semiconductor. A proof-of-principle example is disclosed wherein visible-light excitation generates a high-valent, terminal metal-oxo species relevant to water oxidation catalysis. When coupled with recent advances in water oxidation catalysis, the kinetic rate constants reported provide a framework by which solar water-splitting efficiency can be predicted.

The strategy for generation of high-valent, metal-oxo species with visible light is shown in Figure 1, upper panel. A semiconducting electron acceptor (A), a visible-light-absorbing "sensitizer" (S), and a catalytic metal species (M_{Cat}) are equilibrated with an appropriate redox-active buffer (B) that fixes the catalyst's initial protonation and oxidation states of interest. Light excitation of the sensitizer initiates excited-state electron transfer to the semiconductor, which is known to occur quantitatively on ultrafast time scales under many experimental conditions.[21] "Hole" transfer from the oxidized sensitizer to the catalyst, A-S-M_{cat} + $h\nu$ → A^--S-M^+_{cat}, increases the formal oxidation state of the catalyst by 1, relative to its initial state.

Much of the know-how for the assembly of these components exists in the donor−acceptor literature.[10,22−24] Indeed, a wide variety of organic and inorganic sensitizers are thermodynamically competent for catalyst activation but are themselves kinetically incompetent of significant catalysis. The approach is similar in concept to the flash-quench techniques developed by Gray and co-workers;[1,2] however, the use of the sensitized semiconductor enables quantitative generation of the oxidized sensitizer on sub-nanosecond time scales,[21] and, as is described below, the surface coverage can be controlled to tune the time window for catalysis. A further advantage of this approach is that the $[B^+]/[B^0]$ molar ratio defines the Nernstian potential, whereas the absolute concentration of $[B^+]$ and $[B^0]$ provides a "clock" to reset the catalyst on desired time scales.

The covalently linked sensitizer−catalyst, S-Ru^{II}-OH_2, shown in Figure 1, $[(4,4'\text{-}PO_3H_2)_2bpy)_2Ru(BL)Ru(Mebimpy)(OH_2)]^{4+}$, where BL = 1,2-bis(4′-methyl-[2,2′-bipyridine]-4-yl)ethane, Mebimpy = 2,6-bis(1-methylbenzimidazol-2-yl)-pyridine, and bpy = 2,2′-bipyridine, was utilized in this study. The sensitizer[25] $[(4,4'\text{-}PO_3H_2)_2bpy)_2Ru(dmb)]^{2+}$—where (dmb) = 4,4′′-dimethyl-2,2′-bipyridine—and the catalyst

Received: October 27, 2017
Published: December 18, 2017

DOI: 10.1021/acs.inorgchem.7b02758
Inorg. Chem. 2018, 57, 486−494

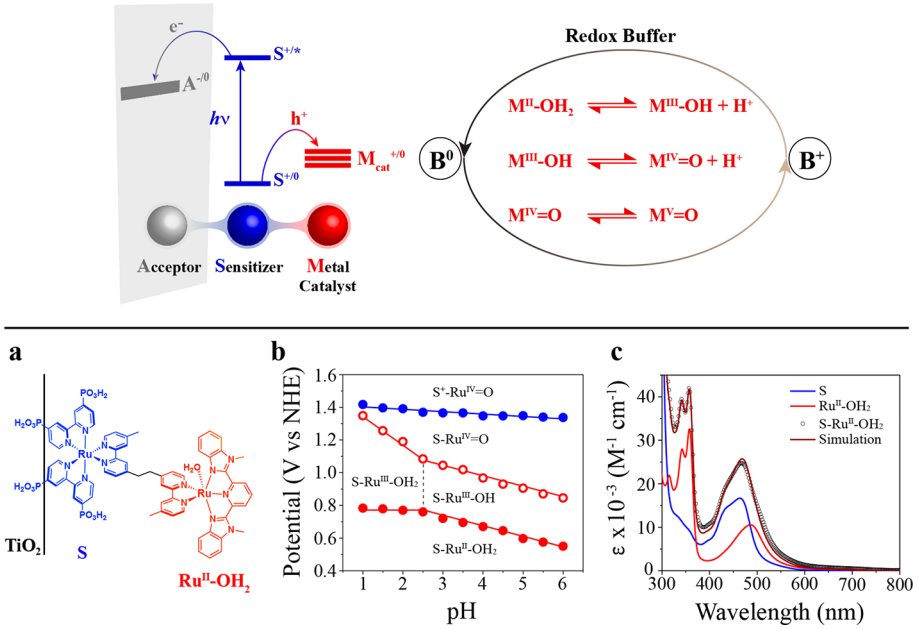

Figure 1. (upper) Demonstration of how a redox mediator B^+/B^0 establishes the initial oxidation state of a transition-metal catalyst M_{cat}; light absorption by a sensitizer S initiates electron transfer to an acceptor A and $1e^-$ oxidation of M_{cat}, whose subsequent reactivity occurs in competition with back electron transfer from the reduced acceptor A^-. (bottom, a) The sensitizer−catalyst under study anchored to nanocrystalline TiO_2 as the acceptor, TiO_2|-S-Ru^{II}-OH_2, (b) Pourbaix diagram of S-Ru^{II}-OH_2 anchored to mesoporous In_2O_3:Sn thin films, and (c) the absorption spectra measured in aqueous 0.1 $HClO_4$ solution for the sensitizer (S), the catalyst (M_{cat}) Ru^{II}-OH_2, and the assembly S-Ru^{II}-OH_2 with an overlaid simulation based on standard addition of the S and M_{cat} spectra.

$[(4,4'\text{-}CH_2PO_3H_2)_2bpy)Ru(Mebimpy)(OH_2)]$[14] have been the subject of previous literature reports,[22,24] and the standard addition of their absorption spectra is in excellent agreement with that measured for S-Ru^{II}-OH_2 consistent with weak electronic coupling through the ethylene linker. The Pourbaix diagram shows that at a pH of 6, a catalyst with a coordinated water molecule in the initial formal oxidation state of II, M^{II}-OH_2, undergoes two sequential, proton-coupled electron-transfer reactions to yield a metal(IV)-oxo species, M^{IV}=O. An additional one-electron oxidation yields a highly reactive M^{V}=O species. All experiments reported herein were performed in aqueous, pH 1 solutions, a pH below the pK_a of Ru^{III}-OH_2. Hence the first catalyst oxidation is not proton-coupled, and both protons are released in the second oxidation. While this $(1e^-, 2H^+)$-redox chemistry has been known for over 20 years,[26−29] this report provides kinetic resolution of Ru(IV)-oxo formation as well as successful demonstration of this strategy for the light-driven generation of a metal-oxo species relevant to solar water oxidation.

EXPERIMENTAL SECTION

Sensitization of Metal Oxide Surfaces. Mesoporous nanocrystalline TiO_2, SnO_2, and tin-doped indium oxide, In_2O_3:Sn, pastes were prepared as previously described.[30−32] The pastes were doctor bladed onto microscopic glass slides or fluorine-doped tin oxide (FTO; Hartford Glass, 15 Ω/sq) and sintered according to standard procedures.[30−32] For saturated surface coverages, the metal oxide substrates were immersed in concentrated solution, $\sim 2.0 \times 10^{-4}$ M, of the sensitizer−catalyst (S-Ru^{II}-OH_2) assembly dissolved in deionized water overnight to give surface coverages of $\sim 8.0 \times 10^{-8}$ mol/cm^2. For experiments performed with one-fourth of the saturation coverage, metal oxide substrates were immersed in diluted aqueous solutions, $\sim 2.0 \times 10^{-5}$ M, of the sensitizer (S), catalyst (Ru^{II}−OH_2), or sensitizer−catalyst (S-Ru^{II}-OH_2) overnight to give surface coverages of $\sim 2.0 \times 10^{-8}$ mol/cm^2. Surface coverages were determined using a modified Beer−Lambert law, $A = \varepsilon \times \Gamma \times 1000$.[33]

After the surface functionalization with dyes, the thin films were rinsed with methanol and with pH 1 water before immersion in a pH 1 solution that was purged with Ar for at least 30 min prior to measurement. The one-electron oxidized catalyst TiO_2|-S-Ru^{III}-OH_2 was prepared by equilibration of TiO_2|-S-Ru^{II}-OH_2 in a 1 mM 1:1 molar ratio of $[Fe^{III}(bpy)_3]^{3+}/[Fe^{II}(bpy)_3]^{2+}$ in pH 1 HNO_3 solution ($E_{1/2}$ = 1 V vs NHE) for at least 10 min.

Atomic Layer Deposition (ALD). A Cambridge NanoTech Savannah S200 instrument was used to deposit a conformal shell of TiO_2 on SnO_2 nanoparticle film cores as described previously at a deposition temperature of 150 °C.[32] In deposition cycles, a 0.3 s pulse of tetrakis(dimethylamido) titanium, $Ti(NMe_2)_4$ (99.999%, Aldrich) was followed by a 20 s exposure in the reactor, a 60 s purge, a 0.02 s pulse of water, a 20 s exposure in the reactor, and a 60 s purge.

Electrochemical and Photophysical Measurements. Spectroelectrochemistry. A standard three-electrode cell was used for electrochemical measurements at room temperature. Mesoporous In_2O_3:Sn thin films deposited onto FTO substrates were sensitized with S-Ru^{II}-OH_2 that served as the working electrode. A platinum wire was used as the counter electrode, and a Ag/AgCl (Pine Instrument) electrode with saturated KCl was the aqueous reference electrode. UV−visible absorption changes for the sensitized films were monitored by a Cary 50 spectrophotometer with a potentiostat (BASi CV 50W) used to apply potential steps. Typically, measurements were performed with 10 mV applied potential steps that were held constant for at least 60 s before a UV−vis absorption spectrum was recorded. In particular, for the Pourbaix diagram shown in Figure 1b, measurements were performed in 0.1 M $NaClO_4$ aqueous solutions with the desired pH adjusted by standard additions of $HClO_4$.

Resonance Raman Spectroscopy. Raman spectra were acquired on a Renishaw inVia Raman Microscope mounted with a Leitz wetzlab 32X/0.30 objective lens. An argon ion laser (Spectra Physics, model 2017) with 514 nm output selected by a laser cleanup filter served as the Raman excitation. The Raman spectroelectrochemistry was performed in a standard electrochemical cell in a three-electrode configuration. For acquisition of the Ru^{IV}=O Raman spectrum, a 1 s

DOI: 10.1021/acs.inorgchem.7b02758
Inorg. Chem. 2018, 57, 486−494

electrochemical pulse at 1.3 V versus Ag/AgCl was applied to generate ITO|-S-Ru^{IV}=O to avoid the full catalytic cycle.

Transient Absorption. Nanosecond transient absorption measurements were performed on a home-built apparatus as previously described.[34]

Comparative Actinometry. Actinometry measurements for injection yield calculations were performed by a previously reported method.[35] A sensitized TiO_2|-RuP ($\Delta\varepsilon$ (450 nm) = −10 000 M^{-1} cm^{-1}), where RuP = $[Ru^{II}(bpy)_2(4,4'\text{-}(PO_3H_2)_2\text{-}2,2'\text{-bipyridine})]^{2+}$, thin film immersed in pH = 1 $HClO_4$ aqueous solution was used as the actinometer with a known quantum yield for excited-state electron injection of unity.[36,37]

Steady-State Photolysis. A Coherent Genesis solid-state laser at 532 nm was expanded to a 2.5 mm diameter spot size and directed at 45° angle onto the sensitized thin film. UV−visible absorption changes were monitored during laser excitation with an AvaSpec ULS2048 UV−vis (Avantes) spectrometer and an Avalight Deuterium/Halogen (Avantes) light source. Data collection was performed by varying detection frequency from 2 to 0.2 Hz. For single wavelength kinetic measurement, at 414 nm, a Varian Cary 50 Bio UV−vis spectrometer was employed in the kinetics mode with an 80 Hz data acquisition. Resonant Raman spectroscopy after steady-state photolysis was measured with the instrument previously described (in this experimental section) under similar conditions of the steady−steady photolysis experiment.

RESULTS AND DISCUSSION

The covalently linked S-Ru^{II}-OH_2 was anchored to tin-doped In_2O_3 (In_2O_3:Sn), TiO_2, or SnO_2/TiO_2 core−shell nanoparticles interconnected in a mesoporous thin film that served as the electron acceptors. The absorption spectra were within experimental error independent of the identity of the metal-oxide support and the surface coverage, where ∼500 sensitizer-catalyst molecules were anchored to each oxide nanocrystallite at saturation surface coverage.[38] Unless otherwise noted, all kinetic data were acquired with one-fourth the saturation surface coverage. The electron-transfer kinetics were sensitive to the nature of the metal oxide as is discussed below.

Figure 2 shows the absorption spectrum of S-Ru^{II}-OH_2 anchored to In_2O_3:Sn and its higher oxidation states. Note that the catalyst absorbs visible light when present in the formal oxidation state of II but absorbs only weakly in the higher oxidation states yet uniquely in the 550−800 nm region. The resonance Raman spectra of the catalyst in the formal oxidation states of II, III, and IV, measured on a In_2O_3:Sn thin film, are

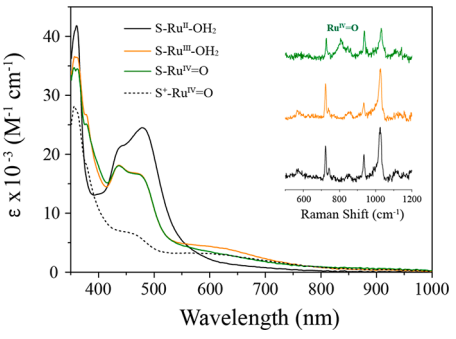

Figure 2. Absorption spectra of S-Ru^{II}-OH_2 anchored to mesoporous In_2O_3:Sn thin film at the indicated higher oxidation states that were obtained by spectroelectrochemical methods. (inset) The resonance Raman spectra color coded to indicate the catalyst redox and protonation state. Highlighted is the assignment of the Ru^{IV}=O vibrational mode observed around 800 cm^{-1}. Experiments were performed in 0.1 M $HClO_4$ aqueous solution.

given in the inset of Figure 2, with a broad resonance centered at 800 cm^{-1} assigned to the Ru^{IV}=O.[39−41]

Pulsed light excitation of TiO_2|-S-Ru^{II}-OH_2 resulted in absorption changes consistent with ultrafast electron injection, $k_{inj} > 1 \times 10^8$ s^{-1}, followed by sub-nanosecond intramolecular electron transfer, $k_{intra} > 1 \times 10^8$ s^{-1}, from the catalyst to the oxidized sensitizer; see eqs 1 and 2 and Figure 3a.

$$TiO_2\text{|-S-}Ru^{II}\text{-}OH_2 + h\nu \rightarrow TiO_2(e^-)\text{|-}S^+\text{-}\mathbf{Ru^{II}}\text{-}\mathbf{OH_2} \quad (k_{inj} > 1 \times 10^8\ s^{-1}) \tag{1}$$

$$TiO_2(e^-)\text{|-}S^+\text{-}\mathbf{Ru^{II}}\text{-}\mathbf{OH_2} \rightarrow TiO_2(e^-)\text{|-S-}\mathbf{Ru^{III}}\text{-}\mathbf{OH_2} \quad (k_{intra} > 1 \times 10^8\ s^{-1}) \tag{2}$$

Clean isosbestic points were observed with normalized spectra that were superimposable, behavior consistent with formation of a single state. Identification of $TiO_2(e^-)$|S-$\mathbf{Ru^{III}}$-$\mathbf{OH_2}$ as being the transient species was also supported by spectral simulations that required standard addition of S-$\mathbf{Ru^{III}}$-$\mathbf{OH_2}$, Figure 3b, necessary to model the experimental data at different time delays, Figure 3a.

The kinetics, eq 3, for charge recombination to the oxidized catalyst

$$TiO_2(e^-)\text{|-S-}\mathbf{Ru^{III}}\text{-}\mathbf{OH_2} \rightarrow TiO_2\text{|-S-}Ru^{II}\text{-}OH_2 \tag{3}$$

were nonexponential and, as shown in the inset, were well-described by the Kohlrausch−Williams−Watts (KWW) kinetic model, Figure 3a inset.[42] Average rate constants[34] for recombination to the oxidized catalyst were significantly smaller than those measured in control experiments with the sensitizer TiO_2|-S or the catalyst directly anchored to the surface through phosphonate linkages, TiO_2|-Ru^{II}P-OH_2, Table 1. Interestingly, recombination dynamics measured for TiO_2|-S and TiO_2|-Ru^{II}P-OH_2 were the same within experimental error, Figure 3a inset. These kinetic observations reveal that the ethylene bridge that links the sensitizer to the catalyst decreases electronic coupling to the distant catalyst, which underlies the sluggish recombination, rather than the ∼500 meV decrease in the thermodynamic driving force. The kinetic data suggests that the injected electrons utilize this bridge "pathway" to reach the remote oxidized catalyst,[34] S-$\mathbf{Ru^{III}}$-$\mathbf{OH_2}$, and growing evidence that interfacial recombination is more sensitive to electronic coupling than to thermodynamic driving force. The corresponding kinetic studies with the SnO_2/TiO_2 core−shell materials maintained an excited-state injection yield near unity with a remarkable ∼25-fold decrease in the average charge recombination rate constant, Figure 3a inset and Table 1.

As described in the experimental section, the one-electron-oxidized catalyst TiO_2|-S-$\mathbf{Ru^{III}}$-$\mathbf{OH_2}$ was prepared and characterized after pulsed laser excitation. The transient spectra shown in Figure 4a were well-modeled by standard addition of the absorption spectra of $\mathbf{S^+}$-$\mathbf{Ru^{III}}$-$\mathbf{OH_2}$ and S-Ru^{II}-OH_2 (Figure 4b), eqs 3 and 4. The mechanism for their formation is understood by recalling that there are hundreds of sensitizer−catalyst molecules anchored to each TiO_2 nanocrystallite. Upon light excitation, only a small percentage of sensitizers absorb light and initiate excited-state

$$TiO_2\text{|-S-}\mathbf{Ru^{III}}\text{-}\mathbf{OH_2} + h\nu \rightarrow TiO_2(e^-)\text{|-}\mathbf{S^+}\text{-}\mathbf{Ru^{III}}\text{-}\mathbf{OH_2} \tag{4}$$

DOI: 10.1021/acs.inorgchem.7b02758
Inorg. Chem. 2018, 57, 486−494

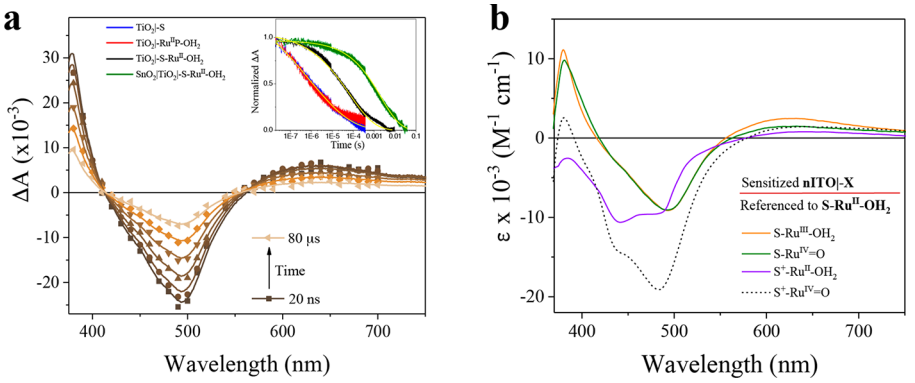

Figure 3. (a) Transient difference spectra measured after pulsed 532 nm excitation of TiO_2|-S-**Ru^{II}-OH_2**. The solid lines overlaid to the data points are simulations based on a least-squares fit to the S-Ru^{III}-OH_2 spectrum (orange) shown in (b). (inset) Normalized kinetic data measured at 490 nm color coded to the indicated sensitized metal oxide thin films with overlaid fits to the KWW function. The excitation irradiance was adjusted to keep the initial number of injected electrons constant. (b) The difference absorption spectra relative to S-Ru^{II}-OH_2 obtained from spectroelectrochemical data shown in Figure 2.

Table 1. Averaged Rate Constants for Charge Recombination[a]

surface ground-state	substrate	$\bar{k}$ (s^{-1})[b]	β	$t_{1/2}$ (s)[c]
|-S[d]	TiO_2	1.9×10^4	0.22	1.2×10^{-6}
|-S-Ru^{II}-OH_2	TiO_2	3.3×10^3	0.36	3.4×10^{-5}
	SnO_2/TiO_2	2.0×10^2	0.47	9.4×10^{-4}
|-S-**Ru^{III}-OH_2**	TiO_2	1.8×10^6	0.36	1.9×10^{-7}
	SnO_2/TiO_2	4.4×10^4	0.47	6.1×10^{-6}

[a]Data acquired at one-fourth saturation surface coverage in aqueous pH 1 solution. [b]Extracted from fits to $A(t) = A_o \times \exp[-(kt)^{\beta}]$; $\bar{k} = [(1/k\beta)\Gamma(1/\beta)]^{-1}$, where Γ is the gamma function. [c]The time required for one-half of the injected electrons to recombine. [d]The recombination kinetics to the oxidized sensitizer and to the oxidized catalyst without a sensitizer present (i.e., |-Ru^{II}P-OH_2) were within experimental error the same; see text for details.

injection. The injected electrons are mobile and rarely undergo geminate recombination but instead preferentially recombine with S-**Ru^{III}-OH_2** species that are present in high numbers on the TiO_2 surface.

The average kinetic rate constant extracted for recombination of the injected electrons with the oxidized catalyst was over 500 times faster when TiO_2|-S-**Ru^{III}-OH_2** was excited relative to TiO_2|-S-**Ru^{II}-OH_2**; see Table 1. This results from the larger number of acceptors present when all the catalysts were preoxidized, whereas equal numbers of injected electrons and oxidized catalysts were present after pulsed excitation of TiO_2|-S-Ru^{II}-OH_2. By employing core−shell SnO_2/TiO_2|-S-**Ru^{III}-OH_2** nanoparticles, the average rate constant for charge recombination reaction measured after pulsed laser excitation relative to that on TiO_2 was decreased by approximately a factor of 10, $k = 4.4 \times 10^4$ s^{-1}. However, under all conditions on the sub-millisecond time scale, there was no evidence for formation of the desired high-valent metal-oxo species.

Interestingly, at low (1/4) saturation coverage, the TiO_2|-**S^+-Ru^{III}-OH_2** and TiO_2|-S-Ru^{II}-OH_2 products were long-lived and did not reset at the 1 Hz repetition rate of the laser. This complication was circumvented by addition of a 1 mM, 4:1 $[Fe^{III}(bpy)_3]^{3+}/[Fe^{II}(bpy)_3]^{2+}$ redox buffer, in the external solution, that ensured recovery of the initial state on time scales less than 1 ms. At saturation surface coverages, data not shown, intermolecular electron transfer mediated by lateral self-

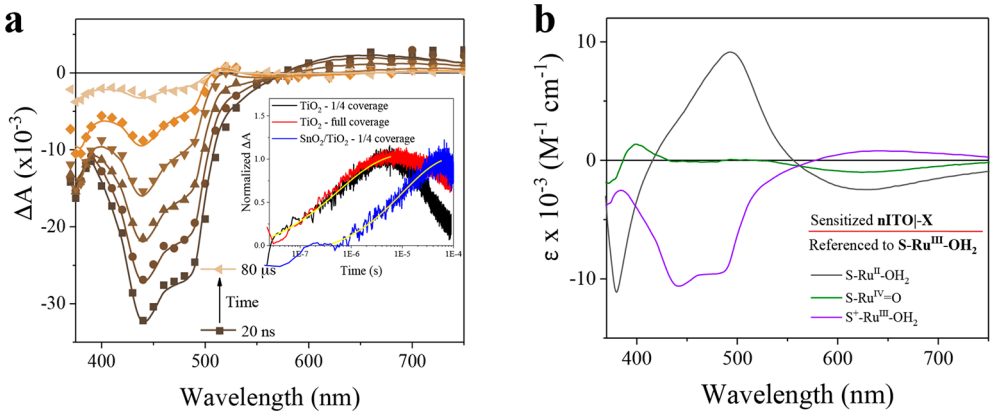

Figure 4. (a) The transient difference spectra measured after pulsed 532 nm excitation of TiO_2|-S-**Ru^{III}-OH_2** with a 1 mM 4:1 ratio of $[Fe^{III/II}(bpy)_3]^{3+/2+}$. The solid lines overlaid on the data points are simulations based on a least-squares fit to all spectra shown in (b). (inset) Normalized kinetic data for the growth of S-Ru^{II}-OH_2 at the indicated metal oxide and surfaces coverages with overlaid fits to the KWW function. Kinetics at one-fourth coverage required use of the redox buffer to recover the initial state in time scales <1 ms; full coverage experiments restored the initial state through intermolecular lateral self-exchange reactions. (b) The difference absorption spectra relative to S-**Ru^{III}-OH_2** obtained from spectroelectrochemical data shown in Figure 2.

DOI: 10.1021/acs.inorgchem.7b02758
Inorg. Chem. 2018, 57, 486−494

exchange reactions across the oxide surface[43] restored the initial TiO_2|-S-$\mathbf{Ru^{III}}$-$\mathbf{OH_2}$ in less than 1 Hz.

In an attempt to ascertain whether the desired Ru^{IV}=O species might form on longer time scales, steady-state illumination experiments of the initially equilibrated TiO_2|-S-$\mathbf{Ru^{III}}$-$\mathbf{OH_2}$ were performed in the absence of an $[Fe^{III/II}(bpy)_3]^{3+/2+}$ redox buffer at low surface coverages that were approximately one-fourth of the saturation value. On the basis of the pulsed laser experiments, such conditions were expected to extend the lifetime of the TiO_2|-$\mathbf{S^+}$-$\mathbf{Ru^{III}}$-$\mathbf{OH_2}$ state, thereby giving more time for generation of the desired metal-oxo species. Indeed, absorption spectra monitored after steady-state 532 nm light excitation revealed intense color changes in the entire visible regions that were absent when saturation surface coverages were utilized. The steady-state spectra were modeled by standard addition of the reference spectra measured by spectroelectrochemistry.

With continued illumination the positive absorption results from the formation of Ru^{II} species, both $S^+ \rightarrow S$ and $TiO_2(e^-)$|-$\mathbf{S-Ru^{III}}$-$\mathbf{OH_2}$ $\rightarrow$ TiO_2|-$\mathbf{S-Ru^{II}}$-$\mathbf{OH_2}$, Figure 5a. This latter

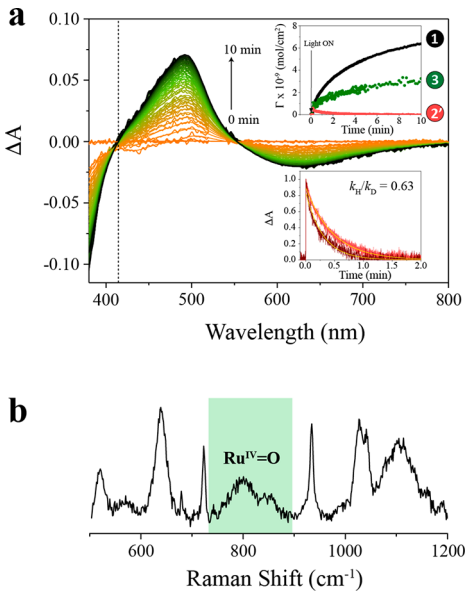

Figure 5. Spectroscopic and kinetic identification of a $1e^-$, $2H^+$ transfer as a rate-limiting step for water oxidation. (a) The absorption changes measured during 10 min of steady-state 532 nm excitation (100 mW/cm^2) of a low surface coverage TiO_2|-S-Ru^{III}-OH_2 thin film at pH 1. The dotted vertical line represents an isosbestic point for TiO_2|-S-Ru^{II}-OH_2. Simulated spectra based on the standard addition of S-Ru^{II}-OH_2, S^+-Ru^{III}-OH_2, and S-Ru^{IV}=O are overlaid to the experimental data. (lower inset) The absorption changes monitored at the 414 nm isosbestic point in H_2O (light coral color) and D_2O (dark coral color) with overlaid fits to a first-order kinetic model, k_H/k_D = 0.63. (upper inset) The concentration profiles obtained from global analysis of the same spectral data. (b) In situ resonance Raman spectrum of TiO_2|-S-Ru^{III}-OH_2 thin film at pH 1 after 10 min of steady-state illumination.

reaction produces the fully reduced species that does not react with TiO_2|-$\mathbf{S^+}$-$\mathbf{Ru^{III}}$-$\mathbf{OH_2}$ on these time scales, because there is no percolation pathway by which they can recombine. We therefore refer to these TiO_2|-$\mathbf{S}$-$\mathbf{Ru^{II}}$-OH_2 species as being "site isolated" from TiO_2|-$\mathbf{S^+}$-$\mathbf{Ru^{III}}$-OH_2. To quantitatively probe the reaction of TiO_2|-$\mathbf{S^+}$-$\mathbf{Ru^{III}}$-OH_2, the 414 nm isosbestic point shown in Figure 5a was monitored. At this wavelength, reduction of the catalyst by injected electrons does not contribute to the absorption change. Analysis at this isosbestic point provides a means for kinetic analysis of the desired ($1e^-$, $2H^+$) reaction, Figure 5a lower inset. The loss of the S^+ contribution at 414 nm is associated with the S^+/S redox chemistry initiated by hole transfer to the catalyst, eq 5. Kinetic measurements at this wavelength revealed a first-order kinetic process performed with absorbed incident irradiances from 30–120 mW/cm^2 that revealed no change in the measured kinetics with k = 0.036 s^{-1}. This first-order behavior is likely to result from water acting as the proton acceptor, which is in large excess compared to the surface-bound chromophore-catalysts assemblies. The rate constant was reproduced in pH 0.8 and 1.2 $HClO_4$ solutions and in pH 1 sulfuric acid solution. To ensure that protons were involved in this reaction, the steady-state photolysis was repeated in heavy water, where an inverse isotope effect of k_H/k_D = 0.63 was found. The details of this are described below. To our knowledge, the data provide the first kinetic resolution of one-electron, two-proton reactivity for ruthenium complexes.

$$TiO_2\text{|-}\mathbf{S^+}\text{-}\mathbf{Ru^{III}}\text{-}\mathbf{OH_2} \rightarrow TiO_2\text{|-S-}\mathbf{Ru^{IV}}\mathbf{=O} + 2H^+ \quad (5)$$

Further evidence of the Ru^{IV}=O came from the appearance of a Raman band at 800 cm^{-1} measured after steady-state illumination, which was in excellent agreement with the spectroelectrochemical Raman data given in Figure 2 and with previous reports.[39−41,44] Compared to the Raman spectrum of S-$\mathbf{Ru^{IV}}$=O generated from spectroelectrochemical measurements, the spectrum in Figure 5b shows additional peaks features at 520, 640, and 1100 cm^{-1} that could be assigned to Ru-peroxide species, given literature values.[44] Additionally, reaction with triphenylphosphine, after the steady-state illumination, resulted in the formation of triphenylphosphine oxide product, which was confirmed by the IR absorption at 1194 cm^{-1}. Such oxide product is observed after electron transfer to the Ru^{IV}=O from a triphenylphosphine coupled to an oxygen-atom transfer step.[6] Below a mechanism for this reactivity is proposed and discussed, Scheme 1.

The spectral data are consistent with the mechanism shown schematically. Light excitation of TiO_2|-S-$\mathbf{Ru^{II}}$-OH_2 (1)

Scheme 1. Proposed Mechanism for Water Oxidation Reaction Catalyzed by the Sensitizer-Catalyst Assembly[a]

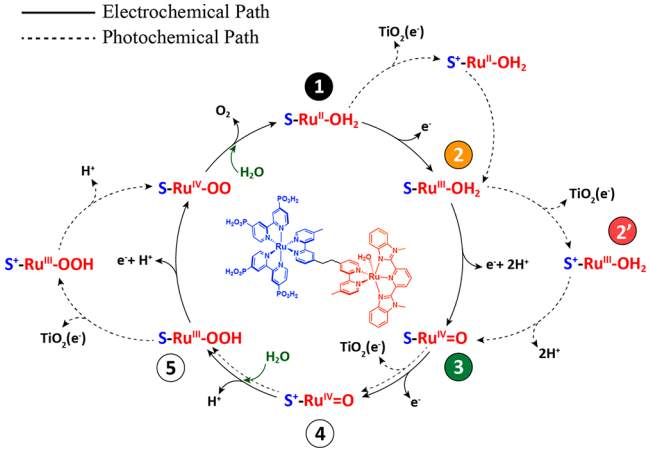

[a]Through an electrochemical path (solid lines) and by a photochemical path (dashed lines).

DOI: 10.1021/acs.inorgchem.7b02758
Inorg. Chem. 2018, 57, 486−494

produced $TiO_2(e^-)$|-S-**Ru^{III}-OH_2** quantitatively within 10 ns. Light excitation of TiO_2|-S-**Ru^{III}-OH_2** (2) resulted in excited-state electron injection to yield $TiO_2(e^-)$|-**S^+-Ru^{III}-OH_2** (2′), which slowly reacted with the same rate constant as the formation of the desired TiO_2|-S-**Ru^{IV}=O** (3), through a $1e^-$, $2H^+$ reaction. This reactivity was enabled by trapping of the injected electron to form TiO_2|-S-Ru^{II}-OH_2 (1) that was site-isolated from TiO_2|-S-**Ru^{IV}=O** (3), given the low surface coverages used. Note that $TiO_2(e^-)$ absorbs only weakly in the visible region and could not be directly quantified. In the absence of other reactivity, injection, trapping, and the ($1e^-$, $2H^+$) reaction would result in equal concentrations of (1) and (3). The inset of Figure 5a shows that this expected stoichiometry was not realized experimentally. Instead, after 10 min of illumination, the concentration of (1) exceeded that of (3) by approximately a factor of 2; that is, ∼31% of the catalysts was present as (1), and 15% was present as (3). This likely occurs because when an appreciable amount of (3), TiO_2|-S-**Ru^{IV}=O**, is present at long illumination times the probability that the sensitizer absorbs light will increase. Excited-state electron injection of TiO_2|-**S***-**Ru^{IV}=O** yields $TiO_2(e^-)$|-**S^+-Ru^{IV}=O** (4) that is reported for related catalysts to rapidly react with water to form TiO_2|-S-**Ru^{III}-OOH** (5).[45−47] Evidence for such species is present in the Raman spectra of Figure 5b, and future $^{18}OH_2$ experiments will allow more definitive assignments.

A complication in the spectral analysis may arise from the fact that compounds (2) and (5) both have a Ru catalyst in the formal oxidation state of III with a bound oxygen ligand. Hence (2) and (5) may have very similar visible absorption spectra. However, we assert that the kinetics can reasonably be assigned to (2′) → (3), rather than to (4) → (5), for three key reasons. First, a vanishingly small fraction of light would be absorbed by (3) at the start of steady-state illumination. Second, the visible absorption spectrum measured 80 μs after laser excitation, in transient absorption experiments, was identical to that measured 500 ms after steady-state photolysis with no detectable amount of (4). Third, the spectral analysis revealed no evidence for the presence of $TiO_2(e^-)$|-**S^+-Ru^{IV}=O**, (4), was present; for every magnitude of S^+ spectral changes, there should be an identical equimolar change in absorbance at wavelengths greater than 550 nm. The advantage of full spectral analysis is that it considers the absorption changes at all wavelengths, and satisfactorily modeling the experimental data did not account for any formation of $TiO_2(e^-)$|-**S^+-Ru^{IV}=O**. Note that the subsequent reactivity, after formation of TiO_2|-S-**Ru^{IV}=O**, requires the existence of S^+ prior to hole transfer to the catalyst. Thus, the mechanism proposed indicates that the formation of the metal-oxo species is the rate-limiting step toward water oxidation at pH 1, while the following steps, including the O−O bond formation, are much faster than the instrument time response, such that formation of S^+ could not be time-resolved. Nonetheless, higher photon fluxes and longer observation times will enhance the probability that (3) absorbs light and thus promotes (4) → (5) reactivity.

Returning now to the ($1e^-$, $2H^+$)-transfer kinetics of the (2′) → (3) reaction, given in eq 5. The slow formation (k = 0.036 s^{-1}) of the Ru^{IV}=O species with ΔG° = −70 meV explains why the reactivity was not observed by transient absorption spectroscopy on millisecond or shorter time scales. Given kinetic competition between the ($1e^-$, $2H^+$)-transfer and charge recombination, the result favors the much faster recombination reaction, even on the core−shell nanostructures. Comparison of this rate constant with literature values is not possible, as this represents the first kinetic resolution of a $1e^-$, $2H^+$ reaction for Ru complexes, although a kinetic isotope effect of 2 was recently reported for an organic 1 e^-, $2H^+$ reaction with strong evidence for a concerted mechanism.[48] Other proton-coupled, electron-transfer reaction mechanisms available include examples where the electrons and protons are transferred in separate steps or in a single, concerted, H atom-transfer step.[23,49−52] A concerted pathway in this transition metal compound involving H_2^+, an unstable species with a bond order of only 1/2, seems unlikely. Hence the observed rate constant is attributed to a composite mechanism that involves discrete electron- and proton-transfer steps.[23]

To gain more insight into the mechanism, the inverse isotope effect of k_H/k_D = 0.63 is considered. The normal isotope effects usually measured correspond to cases where breaking the O−H bond is the rate-determining step.[51] The lack of a primary isotope effect clearly indicates that cleavage of an O−H bond was not rate limiting and implicates electron transfer. However, electron transfer through this same bridging ligand at essentially the same driving force has been shown to occur on a sub-nanosecond time scale in both fluid solution and at TiO_2 interfaces.[53,54] Hence electron transfer is not likely to be the rate-determining step. Instead, a pre-equilibrium is proposed in which interfacial water molecules associate with the coordinated water in TiO_2|-**S^+-Ru^{III}-OH_2** prior to proton or electron transfer. The details of this solvation are unknown; however, the sterics about the metal's active site are expected to be sensitive to the larger deuterium atoms resulting in a more rapid reaction. We note that inverse isotope effects of this same magnitude have been reported for the electrochemical oxidation of water with Ni and Co electrodes.[55] The report of inverse isotope effects of similar magnitude at electrode surfaces suggests that the specific organization of interfacial water is also critical to the generation of the high-valent, metal-oxo catalysts that drive water oxidation. Water is the likely proton acceptor for the desired reaction, but it is limited by its acid−base properties with a pK_a = 15.7.

The kinetic data explain why water oxidation is inefficient for these materials in acidic media. Formation of the Ru^{IV}=O is at least 3 orders of magnitude slower than charge recombination resulting in less than 1% yields of TiO_2|-S-**Ru^{IV}=O**. As described above, this is likely rate-determining in water photo-oxidation, as excited-state injection yields $TiO_2(e^-)$|-**S^+-Ru^{IV}=O** with no proton barrier for the intramolecular generation of the putative Ru^V=O that is so reactive that it has never been directly observed.[46] Furthermore, there is strong evidence that TiO_2|-**S^+-Ru^{IV}=O** would oxidize water directly.[45−47]

Efficient water oxidation requires catalytic turnover frequencies greater than the 4.4×10^4 s^{-1} values measured for charge recombination in the core−shell oxides. Under more alkaline conditions, and in the presence of buffer bases as proton acceptors, related catalysts[56] have turnover frequencies of 50 000 s^{-1}, which indicates an ∼50% quantum yield with the kinetic data reported herein. However, interfacial charge recombination is pH sensitive and becomes slower at higher pH values,[57,58] and there is good reason to believe that alternative bridge units that link the catalyst to the sensitizer can slow unwanted recombination[34] even further resulting in quantitative yields for each of the catalyst's activation steps and hence for water oxidation on an absorbed-photon basis.

The data raise questions of whether lateral intermolecular charge transfer between the catalysts is beneficial or detrimental

DOI: 10.1021/acs.inorgchem.7b02758
Inorg. Chem. 2018, 57, 486−494

to water oxidation. The ∼2 orders-of-magnitude increase in the charge recombination rate constant for the second oxidation step almost certainly reflects the fact that every single catalyst was present as TiO_2|-S-$\mathbf{Ru^{III}}$-$\mathbf{OH_2}$ and hence available to accept injected electrons. Furthermore, fast lateral self-exchange reactions at saturation surface coverages resulted in the formation of ground-state products before the desired reaction chemistry had a chance to occur. Therefore, in this study, site isolation of the catalysts inhibited recombination and enabled the desired Ru^{IV}═O species to form. Literature reports of water oxidation catalysis with buffer bases that accept protons from the coordinated water with the kinetic data reported herein indicate that water oxidation yields well over 50% on an absorbed-photon basis are possible. The decreased light absorption that would result from the lower surface coverage could, in principle, be compensated by thicker mesoporous thin films.

CONCLUSION

In summary, an interfacial approach to the photogeneration of high-valent, metal-oxo species has been described. A redox buffer enables the catalyst oxidation and protonation states to be established prior to light excitation on a wideband gap oxide surface. The catalyst's surface coverage and the redox buffer were independently tuned to reset the catalyst on desired time scales. Weak electronic coupling through a methylene spacer resulted in slow charge recombination of the injected electron with the oxidized catalyst. The kinetic data also revealed an order-of-magnitude decrease in average charge recombination rate constants that result from having a SnO_2 core with a TiO_2 shell relative to TiO_2 alone. A novel trapping process present at subpercolation surface coverages increased the lifetime of the oxidized catalyst dramatically and, in the absence of the redox buffer, allowed the first application of this approach for the realization of a light-driven, ($1e^-$, $2H^+$)-reaction to yield a Ru^{IV}═O species with $k = 0.036\ s^{-1}$, an inverse isotope effect of $k_H/k_D = 0.63$ with $\Delta G^\circ = -70$ meV. The metal-oxo product was found to be remarkably stable in pH 1 solution, but there was evidence for a reaction with water when the covalently linked sensitizer was photo-oxidized. The nearly 2 orders-of-magnitude increase in recombination when all the catalysts were preoxidized by one electron indicates that site isolation of catalysts with high turnover frequencies will enable more efficient light-driven water-oxidation.

AUTHOR INFORMATION

Corresponding Authors

*E-mail: gjmeyer@email.unc.edu. (G.J.M.)
*E-mail: tjmeyer@email.unc.edu. (T.J.M.)

ORCID

Ke Hu: 0000-0002-0240-7192
Thomas J. Meyer: 0000-0002-7006-2608
Gerald J. Meyer: 0000-0002-4227-6393

Author Contributions

§Contributed equally.

Notes

The authors declare no competing financial interest.

ACKNOWLEDGMENTS

The research was supported solely by the UNC EFRC: Center for Solar Fuels, an Energy Frontier Research Center funded by the U.S. Department of Energy, Office of Science, Basic Energy Sciences, under Award No. DE-SC0001011.

REFERENCES

(1) Berglund, J.; Pascher, T.; Winkler, J. R.; Gray, H. B. Photoinduced Oxidation of Horseradish Peroxidase. *J. Am. Chem. Soc.* **1997**, *119*, 2464−2469.
(2) Low, D. W.; Winkler, J. R.; Gray, H. B. Photoinduced Oxidation of Microperoxidase-8: Generation of Ferryl and Cation-Radical Porphyrins. *J. Am. Chem. Soc.* **1996**, *118*, 117−120.
(3) Krebs, C.; Galonić Fujimori, D.; Walsh, C. T.; Bollinger, J. M. Non-Heme Fe(IV)−Oxo Intermediates. *Acc. Chem. Res.* **2007**, *40*, 484−492.
(4) Que, L., Jr; Tolman, W. B. Biologically Inspired Oxidation Catalysis. *Nature* **2008**, *455*, 333−340.
(5) Fukuzumi, S.; Kojima, T.; Lee, Y.-M.; Nam, W. High-Valent Metal-Oxo Complexes Generated in Catalytic Oxidation Reactions Using Water as an Oxygen Source. *Coord. Chem. Rev.* **2017**, *333*, 44−56.
(6) Moyer, B. A.; Meyer, T. J. Oxobis(2,2′-bipyridine)-pyridineruthenium(IV) ion, $[(bpy)_2(py)Ru = O]^{2+}$. *J. Am. Chem. Soc.* **1978**, *100*, 3601−3603.
(7) Gersten, S. W.; Samuels, G. J.; Meyer, T. J. Catalytic Oxidation of Water by an Oxo-Bridged Ruthenium Dimer. *J. Am. Chem. Soc.* **1982**, *104*, 4029−4030.
(8) Concepcion, J. J.; Jurss, J. W.; Brennaman, M. K.; Hoertz, P. G.; Patrocinio, A. O. T.; Murakami Iha, N. Y.; Templeton, J. L.; Meyer, T. J. Making Oxygen with Ruthenium Complexes. *Acc. Chem. Res.* **2009**, *42*, 1954−1965.
(9) Kärkäs, M. D.; Verho, O.; Johnston, E. V.; Åkermark, B. Artificial Photosynthesis: Molecular Systems for Catalytic Water Oxidation. *Chem. Rev.* **2014**, *114*, 11863−12001.
(10) Blakemore, J. D.; Crabtree, R. H.; Brudvig, G. W. Molecular Catalysts for Water Oxidation. *Chem. Rev.* **2015**, *115*, 12974−13005.
(11) Gunay, A.; Theopold, K. H. C−H Bond Activations by Metal Oxo Compounds. *Chem. Rev.* **2010**, *110*, 1060−1081.
(12) Groves, J. T. Enzymatic C-H Bond Activation: Using Push to Get Pull. *Nat. Chem.* **2014**, *6*, 89−91.
(13) Fukuzumi, S. Electron Transfer and Catalysis With High-Valent Metal-Oxo Complexes. *Dalton Trans.* **2015**, *44*, 6696−6705.
(14) Concepcion, J. J.; Tsai, M.-K.; Muckerman, J. T.; Meyer, T. J. Mechanism of Water Oxidation by Single-Site Ruthenium Complex Catalysts. *J. Am. Chem. Soc.* **2010**, *132*, 1545−1557.
(15) Zhang, M.; de Respinis, M.; Frei, H. Time-Resolved Observations of Water Oxidation Intermediates on a Cobalt Oxide Nanoparticle Catalyst. *Nat. Chem.* **2014**, *6*, 362−367.
(16) Zandi, O.; Hamann, T. W. Determination of Photo-electrochemical Water Oxidation Intermediates on Haematite Electrode Surfaces Using Operando Infrared Spectroscopy. *Nat. Chem.* **2016**, *8*, 778−783.
(17) Fukuzumi, S.; Jung, J.; Yamada, Y.; Kojima, T.; Nam, W. Homogeneous and Heterogeneous Photocatalytic Water Oxidation by Persulfate. *Chem. - Asian J.* **2016**, *11*, 1138−1150.
(18) Lewandowska-Andralojc, A.; Polyansky, D. E.; Zong, R.; Thummel, R. P.; Fujita, E. Enabling Light-Driven Water Oxidation Via a Low-Energy Ru^{IV}═O Intermediate. *Phys. Chem. Chem. Phys.* **2013**, *15*, 14058−14068.
(19) Wasser, I. M.; Fry, H. C.; Hoertz, P. G.; Meyer, G. J.; Karlin, K. D. Photochemical Organic Oxidations and Dechlorinations with a μ-Oxo Bridged Heme/Non-Heme Diiron Complex. *Inorg. Chem.* **2004**, *43*, 8272−8281.
(20) Richman, R. M.; Peterson, M. W. Photodisproportionation of μ-Oxo-bis[(tetraphenylporphinato)iron(III)]. *J. Am. Chem. Soc.* **1982**, *104*, 5795−5796.
(21) Zigler, D. F.; Morseth, Z. A.; Wang, L.; Ashford, D. L.; Brennaman, M. K.; Grumstrup, E. M.; Brigham, E. C.; Gish, M. K.; Dillon, R. J.; Alibabaei, L.; Meyer, G. J.; Meyer, T. J.; Papanikolas, J. M. Disentangling the Physical Processes Responsible for the Kinetic

DOI: 10.1021/acs.inorgchem.7b02758
Inorg. Chem. 2018, 57, 486−494

Complexity in Interfacial Electron Transfer of Excited Ru(II) Polypyridyl Dyes on TiO_2. *J. Am. Chem. Soc.* **2016**, *138*, 4426−4438.
(22) Brennaman, M. K.; Dillon, R. J.; Alibabaei, L.; Gish, M. K.; Dares, C. J.; Ashford, D. L.; House, R. L.; Meyer, G. J.; Papanikolas, J. M.; Meyer, T. J. Finding the Way to Solar Fuels with Dye Sensitized Photoelectrosynthesis Cells. *J. Am. Chem. Soc.* **2016**, *138*, 13085−13102.
(23) Weinberg, D. R.; Gagliardi, C. J.; Hull, J. F.; Murphy, C. F.; Kent, C. A.; Westlake, B. C.; Paul, A.; Ess, D. H.; McCafferty, D. G.; Meyer, T. J. Proton-Coupled Electron Transfer. *Chem. Rev.* **2012**, *112*, 4016−4093.
(24) Ashford, D. L.; Gish, M. K.; Vannucci, A. K.; Brennaman, M. K.; Templeton, J. L.; Papanikolas, J. M.; Meyer, T. J. Molecular Chromophore−Catalyst Assemblies for Solar Fuel Applications. *Chem. Rev.* **2015**, *115*, 13006−13049.
(25) Ashford, D. L.; Song, W.; Concepcion, J. J.; Glasson, C. R. K.; Brennaman, M. K.; Norris, M. R.; Fang, Z.; Templeton, J. L.; Meyer, T. J. Photoinduced Electron Transfer in a Chromophore−Catalyst Assembly Anchored to TiO_2. *J. Am. Chem. Soc.* **2012**, *134*, 19189−19198.
(26) Binstead, R. A.; Meyer, T. J. Hydrogen-Atom Transfer Between Metal Complex Ions in Solution. *J. Am. Chem. Soc.* **1987**, *109*, 3287−3297.
(27) Yagi, M.; Tajima, S.; Komi, M.; Yamazaki, H. Highly Active and Tunable catalysts for O_2 Evolution From Water Based on Mononuclear Ruthenium(II) Monoaquo Complexes. *Dalton Trans.* **2011**, *40*, 3802−3804.
(28) Patel, J.; Majee, K.; Padhi, S. K. $[Ru^{V}(NCN\text{-}Me)(bpy)(=O)]^{3+}$ Mediated Efficient Photo-driven Water Oxidation. *RSC Adv.* **2016**, *6*, 61959−61965.
(29) Ryan, D. M.; Coggins, M. K.; Concepcion, J. J.; Ashford, D. L.; Fang, Z.; Alibabaei, L.; Ma, D.; Meyer, T. J.; Waters, M. L. Synthesis and Electrocatalytic Water Oxidation by Electrode-Bound Helical Peptide Chromophore−Catalyst Assemblies. *Inorg. Chem.* **2014**, *53*, 8120−8128.
(30) Argazzi, R.; Bignozzi, C. A.; Heimer, T. A.; Castellano, F. N.; Meyer, G. J. Enhanced Spectral Sensitivity from Ruthenium(II) Polypyridyl Based Photovoltaic Devices. *Inorg. Chem.* **1994**, *33*, 5741−5749.
(31) Farnum, B. H.; Morseth, Z. A.; Lapides, A. M.; Rieth, A. J.; Hoertz, P. G.; Brennaman, M. K.; Papanikolas, J. M.; Meyer, T. J. Photoinduced Interfacial Electron Transfer Within a Mesoporous Transparent Conducting Oxide Film. *J. Am. Chem. Soc.* **2014**, *136*, 2208−2211.
(32) Alibabaei, L.; Sherman, B. D.; Norris, M. R.; Brennaman, M. K.; Meyer, T. J. Visible Photoelectrochemical Water Wplitting into H_2 and O_2 in a Dye-Sensitized Photoelectrosynthesis Cell. *Proc. Natl. Acad. Sci. U. S. A.* **2015**, *112*, 5899−5902.
(33) Trammell, S. A.; Meyer, T. J. Diffusional Mediation of Surface Electron Transfer on TiO_2. *J. Phys. Chem. B* **1999**, *103*, 104−107.
(34) Hu, K.; Blair, A. D.; Piechota, E. J.; Schauer, P. A.; Sampaio, R. N.; Parlane, F. G. L.; Meyer, G. J.; Berlinguette, C. P. Kinetic Pathway for Interfacial Electron Transfer From a Semiconductor to a Molecule. *Nat. Chem.* **2016**, *8*, 853−859.
(35) Bergeron, B. V.; Kelly, C. A.; Meyer, G. J. Thin Film Actinometers for Transient Absorption Spectroscopy: Applications to Dye-Sensitized Solar Cells. *Langmuir* **2003**, *19*, 8389−8394.
(36) Hanson, K.; Losego, M. D.; Kalanyan, B.; Parsons, G. N.; Meyer, T. J. Stabilizing Small Molecules on Metal Oxide Surfaces Using Atomic Layer Deposition. *Nano Lett.* **2013**, *13*, 4802−4809.
(37) Hanson, K.; Brennaman, M. K.; Ito, A.; Luo, H.; Song, W.; Parker, K. A.; Ghosh, R.; Norris, M. R.; Glasson, C. R. K.; Concepcion, J. J.; Lopez, R.; Meyer, T. J. Structure−Property Relationships in Phosphonate-Derivatized, Ru^{II} Polypyridyl Dyes on Metal Oxide Surfaces in an Aqueous Environment. *J. Phys. Chem. C* **2012**, *116*, 14837−14847.
(38) O'Regan, B. C.; Durrant, J. R. Kinetic and Energetic Paradigms for Dye-Sensitized Solar Cells: Moving from the Ideal to the Real. *Acc. Chem. Res.* **2009**, *42*, 1799−1808.
(39) Yamada, H.; Koike, T.; Hurst, J. K. Water Exchange Rates in the Diruthenium μ-Oxo Ion cis,cis-$[(bpy)_2Ru(OH_2)]_2O^{4+}$. *J. Am. Chem. Soc.* **2001**, *123*, 12775−12780.
(40) Paeng, I. R.; Nakamoto, K. Resonance Raman Spectra of Reaction Intermediates in Oxidation Process of Ruthenium(II) and Iron(II) Porphyrins. *J. Am. Chem. Soc.* **1990**, *112*, 3289−3297.
(41) Yamada, H.; Hurst, J. K. Resonance Raman, Optical Spectroscopic, and EPR Characterization of the Higher Oxidation States of the Water Oxidation Catalyst, cis,cis-$[(bpy)_2Ru(OH_2)]_2O^{4+}$. *J. Am. Chem. Soc.* **2000**, *122*, 5303−5311.
(42) Williams, G.; Watts, D. C. Non-Symmetrical Dielectric Relaxation Behaviour Arising From a Simple Empirical Decay Function. *Trans. Faraday Soc.* **1970**, *66*, 80−85.
(43) Hu, K.; Meyer, G. J. Lateral Intermolecular Self-Exchange Reactions for Hole and Energy Transport on Mesoporous Metal Oxide Thin Films. *Langmuir* **2015**, *31*, 11164−11178.
(44) Polyansky, D. E.; Muckerman, J. T.; Rochford, J.; Zong, R.; Thummel, R. P.; Fujita, E. Water Oxidation by a Mononuclear Ruthenium Catalyst: Characterization of the Intermediates. *J. Am. Chem. Soc.* **2011**, *133*, 14649−14665.
(45) Alibabaei, L.; Brennaman, M. K.; Norris, M. R.; Kalanyan, B.; Song, W.; Losego, M. D.; Concepcion, J. J.; Binstead, R. A.; Parsons, G. N.; Meyer, T. J. Solar Water Splitting in a Molecular Photoelectrochemical Cell. *Proc. Natl. Acad. Sci. U. S. A.* **2013**, *110*, 20008−20013.
(46) Pushkar, Y.; Moonshiram, D.; Purohit, V.; Yan, L.; Alperovich, I. Spectroscopic Analysis of Catalytic Water Oxidation by $[Ru^{II}(bpy)(tpy)H_2O]_2^{+}$ Suggests That Ru^{V}=O Is Not a Rate-Limiting Intermediate. *J. Am. Chem. Soc.* **2014**, *136*, 11938−11945.
(47) Norris, M. R.; Concepcion, J. J.; Fang, Z.; Templeton, J. L.; Meyer, T. J. Low-Overpotential Water Oxidation by a Surface-Bound Ruthenium-Chromophore−Ruthenium-Catalyst Assembly. *Angew. Chem., Int. Ed.* **2013**, *52*, 13580−13583.
(48) Huynh, M. T.; Mora, S. J.; Villalba, M.; Tejeda-Ferrari, M. E.; Liddell, P. A.; Cherry, B. R.; Teillout, A.-L.; Machan, C. W.; Kubiak, C. P.; Gust, D.; Moore, T. A.; Hammes-Schiffer, S.; Moore, A. L. Concerted One-Electron Two-Proton Transfer Processes in Models Inspired by the Tyr-His Couple of Photosystem II. *ACS Cent. Sci.* **2017**, *3*, 372−380.
(49) Hammes-Schiffer, S. Theory of Proton-Coupled Electron Transfer in Energy Conversion Processes. *Acc. Chem. Res.* **2009**, *42*, 1881−1889.
(50) Gagliardi, C. J.; Wang, L.; Dongare, P.; Brennaman, M. K.; Papanikolas, J. M.; Meyer, T. J.; Thompson, D. W. Direct Observation of Light-Driven, Concerted Electron−Proton Transfer. *Proc. Natl. Acad. Sci. U. S. A.* **2016**, *113*, 11106.
(51) Nishida, Y.; Morimoto, Y.; Lee, Y.-M.; Nam, W.; Fukuzumi, S. Effects of Proton Acceptors on Formation of a Non-Heme Iron(IV)−Oxo Complex via Proton-Coupled Electron Transfer. *Inorg. Chem.* **2013**, *52*, 3094−3101.
(52) Chen, Z.; Vannucci, A. K.; Concepcion, J. J.; Jurss, J. W.; Meyer, T. J. Proton-Coupled Electron Transfer at Modified Electrodes by Multiple Pathways. *Proc. Natl. Acad. Sci. U. S. A.* **2011**, *108*, E1461−E1469.
(53) Indelli, M. T.; Bignozzi, C. A.; Harriman, A.; Schoonover, J. R.; Scandola, F. Four Intercomponent Processes in a Ru(II)-Rh(III) Polypyridine Dyad: Electron Transfer from Excited Donor, Electron Transfer to Excited Acceptor, Charge Recombination, and Electronic Energy Transfer. *J. Am. Chem. Soc.* **1994**, *116*, 3768−3779.
(54) Kleverlaan, C. J.; Indelli, M. T.; Bignozzi, C. A.; Pavanin, L.; Scandola, F.; Hasselman, G. M.; Meyer, G. J. Stepwise Charge Separation in Heterotriads. Binuclear Ru(II)−Rh(III) Complexes on Nanocrystalline Titanium Dioxide. *J. Am. Chem. Soc.* **2000**, *122*, 2840−2849.
(55) Tse, E. C. M.; Hoang, T. T. H.; Varnell, J. A.; Gewirth, A. A. Observation of an Inverse Kinetic Isotope Effect in Oxygen Evolution Electrochemistry. *ACS Catal.* **2016**, *6*, 5706−5714.
(56) Matheu, R.; Ertem, M. Z.; Benet-Buchholz, J.; Coronado, E.; Batista, V. S.; Sala, X.; Llobet, A. Intramolecular Proton Transfer

DOI: 10.1021/acs.inorgchem.7b02758
Inorg. Chem. 2018, 57, 486−494

Boosts Water Oxidation Catalyzed by a Ru Complex. *J. Am. Chem. Soc.* **2015**, *137*, 10786−10795.
(57) Knauf, R. R.; Brennaman, M. K.; Alibabaei, L.; Norris, M. R.; Dempsey, J. L. Revealing the Relationship between Semiconductor Electronic Structure and Electron Transfer Dynamics at Metal Oxide−Chromophore Interfaces. *J. Phys. Chem. C* **2013**, *117*, 25259−25268.
(58) Brennaman, M. K.; Patrocinio, A. O. T.; Song, W.; Jurss, J. W.; Concepcion, J. J.; Hoertz, P. G.; Traub, M. C.; Murakami Iha, N. Y.; Meyer, T. J. Interfacial Electron Transfer Dynamics Following Laser Flash Photolysis of $[Ru(bpy)_2((4,4'\text{-}PO_3H_2)_2bpy)]^{2+}$ in TiO_2 Nanoparticle Films in Aqueous Environments. *ChemSusChem* **2011**, *4*, 216−227.

DOI: 10.1021/acs.inorgchem.7b02758
Inorg. Chem. 2018, 57, 486−494